

# Rapid transition from primary to secondary crust building on the Moon explained by mantle overturn.

Tabb Prissel (✉ [tabb.c.prissel@nasa.gov](mailto:tabb.c.prissel@nasa.gov))

Jacobs-JETS

Nan Zhang

Peking University <https://orcid.org/0000-0001-5160-5630>

Colin Jackson

Tulane University

Haoyuan Li

Peking University

---

## Article

### Keywords:

**Posted Date:** March 17th, 2022

**DOI:** <https://doi.org/10.21203/rs.3.rs-1339976/v1>

**License:** © ⓘ This work is licensed under a Creative Commons Attribution 4.0 International License.

[Read Full License](#)

---

**Version of Record:** A version of this preprint was published at Nature Communications on August 17th, 2023. See the published version at <https://doi.org/10.1038/s41467-023-40751-7>.

# Abstract

Geochronology indicates a rapid transition from primary to secondary crust building on the Moon. However, a lack of consensus remains regarding the operative mechanisms responsible for generation of early secondary magmas and their global extent. This study tests the hypothesis that the earliest secondary crust (Mg-suite rocks) formed as a direct result of density-driven cumulate mantle overturn. To do this, we advance 3-D mantle convection models to predict the extent of lower mantle melting induced by cumulate overturn. In contrast to previous suggestions, our results demonstrate that mantle overturn alone can simultaneously explain the abundance, timing, and spatial extent of early secondary crust building without contributions from other energy sources, i.e., lunar KREEP (potassium, rare earth elements, phosphorus, radiogenic U, Th). We propose that gravitational instabilities in magma ocean cumulate piles are major driving forces for the onset of mantle convection and initial secondary crust building on differentiated bodies.

## 1. Introduction

Akin to the theory of plate tectonics on Earth, the magma ocean and cumulate mantle overturn (CMO) hypotheses work in concert as the guiding paradigms for the formation and redistribution of mantle and crustal material on terrestrial bodies<sup>1,2</sup>. These concepts were largely developed through exploration of the Moon, and its rock record still provides the most direct evidence for the lunar magma ocean (LMO) and CMO epochs. Here the lunar magnesian-suite of samples stand out (Mg-suite: dunite, pink spinel troctolite, troctolite, norite, gabbronorite). Their primitive olivine compositions anchor the Mg-suite mantle source to initially deep-seated primary LMO cumulates, and its presence within the lunar crust therefore demands mobilization of said cumulates toward the surface via CMO<sup>3-7</sup>. Geochronology indicates that Mg-suite petrogenesis, and by extension CMO, occurred near-contemporaneously with LMO solidification<sup>8,9</sup>. Thus, the Mg-suite plays a pivotal role in unraveling the magmatic transition from primary to secondary crust building on the Moon. Despite these critical links to early lunar evolution, a lack of consensus remains regarding the operative mechanisms responsible for generation of early secondary magmas and their global extent<sup>10-13</sup>.

Confounding the origin of Mg-suite is that samples returned by the Apollo missions contain elevated concentrations of trace elements associated with a KREEP component (potassium, rare earth elements, phosphorus)<sup>10</sup>. The KREEP signature observed in Mg-suite samples is surprising because the formation of KREEP is tied to the final stages of LMO crystallization, contrasting with the primitive origins demanded by their major element composition. Determining the role of KREEP during Mg-suite petrogenesis is important because its high concentrations of U, Th, and K make KREEP a major source for radiogenic heat in the magmatic evolution of the Moon<sup>14,15</sup>. KREEP-induced melting was recently proposed to be the primary mechanism for explaining the observed lunar crustal dichotomy<sup>12</sup>, potentially determining the production and distribution of Mg-suite magmatism<sup>4,5,12</sup>.

Mounting lines of evidence now call into question the importance of KREEP in Mg-suite petrogenesis. KREEP-poor lunar meteorites with a chemical affinity to Mg-suite are documented<sup>10,16-18</sup>, thermochemical models demonstrate no need for KREEP to produce Mg-suite magmas derived from primary LMO cumulates<sup>11</sup>, and remote sensing observations identify Mg-suite locations across the lunar surface<sup>19-21</sup>, far beyond the Procellarum KREEP Terrane (PKT) where KREEP appears most concentrated. If KREEP is not a primary driver of Mg-suite petrogenesis, CMO rises as the central geologic process for initiating secondary crust building on the Moon. And although recent geochemical links between Mg-suite and CMO have been forwarded<sup>11</sup>, a KREEP-free relationship between Mg-suite and CMO remains untested by modern dynamical models of early lunar mantle convection. Moreover, the last decade has delivered advances in geochronology and global mineralogical analyses that present new challenges to the CMO hypothesis, and these are discussed below.

First, geochronological work identifies near-concordant dates for putative primary lunar crust (a proxy for LMO solidification) and secondary Mg-suite samples<sup>8,9,22-26</sup>. The maximum disparity between concordant crystallization ages of the primary lunar crust ( $4359 \pm 9$  Ma) and Mg-suite rocks ( $4340 \pm 9$  Ma) dictates that CMO-induced origin models must produce Mg-suite magmas within  $\sim 37$  Myrs of LMO solidification<sup>8</sup>. CMO-induced melting of the Mg-suite source must also have been short-lived ( $< 18$  Myrs) to explain the small variance in crystallization ages between robustly dated Mg-suite rocks<sup>8</sup>.

Second, combined petrological and remote sensing studies also now constrain the global distribution of Mg-suite rock types<sup>20,21,27-30</sup>. From these studies, the Mg-suite appears to be broadly distributed across the Moon and not isolated within a single regional terrane (Fig. 1). The presence of KREEP-poor meteorites with a chemical affinity to Mg-suite<sup>10,16-18</sup>, likely sourced from localities outside of the PKT, provide ground-truth to the global extent implied by remote observations. This broad distribution of Mg-suite suggests that CMO operated as a global emplacement process<sup>28</sup>. Although Mg-suite rocks appear widespread, they are estimated to comprise  $\sim 6-30$  vol.% of the total lunar crust<sup>19,31</sup>, constraining the extent of melting in associated petrogenetic models.

Taken together, the emerging picture is that the Mg-suite formed near contemporaneously with LMO solidification during a short magmatic interval, is broadly distributed across the Moon, and constitutes a modest fraction of the lunar crust. Here, we employ a recently developed three-dimensional mantle convection model<sup>32</sup> to examine the spatial and temporal distribution of mantle melting produced by the upwelling return flow of primary magma ocean cumulates in response to CMO. We further advance the existing geodynamic model by integrating available data from geochronology, petrologic studies, and orbital spacecraft, to determine if **i)** CMO-induced decompression melting is capable of producing sufficient volumes of Mg-suite material, **ii)** the magmatic duration of CMO-induced melting is consistent with the small variance observed in the most reliable Mg-suite crystallization ages, and **iii)** the onset of CMO-induced melting can reconcile the apparent brief formation interval between primary and secondary crust formation on the Moon. The global distribution of melts stemming from each case is then evaluated to test whether **iv)** a CMO origin can simultaneously satisfy the current spatial distribution of

global Mg-suite exposures. In so doing, we identify physical properties of lunar CMO that ultimately satisfy modern observations.

## 2. Results

We investigate the thermochemical evolution of density-driven cumulate mantle overturn and convective return flow using a numerical three-dimensional model of spherical geometry<sup>32</sup> and test the effects of ilmenite-bearing cumulate (IBC) thickness and viscosity contrast between the IBC layer and underlying mantle. Except for the additional consideration of mantle layering (described further in our methods), our model is the same as that reported in<sup>32</sup>. Results are assessed using the following constraints to determine which models are most consistent with the natural observations (with additional discussion provided in our methods).

- Constraint 1 (Mg-suite volume) is defined by the estimated amount of Mg-suite material within the lunar crust, or  $\sim 6\text{--}30$  vol.% of the total lunar crust<sup>19,31</sup>.
- Constraint 2 (magmatic duration) is constrained by the estimated duration of Mg-suite magmatism based on concordant dating of Mg-suite samples. The magmatic duration is therefore constrained by the variation of concordant Mg-suite dates, or  $\pm 9$  Myrs<sup>8</sup>.
- Constraint 3 (formation interval) considers the interval of time between primary and secondary crust building. This constraint is defined by the maximum interval of time between the closure ages of ferroan anorthosites and the crystallization ages of secondary Mg-suite samples (including the respective variance associated with each age), or  $\sim 37$  Myrs<sup>8</sup>.
- Constraints 4 and 5 (exposure and farthest neighbor) account for the global distribution of Mg-Suite detections as constrained by mineralogical analyses from orbital spacecraft. Considering the data set of<sup>21</sup>, we estimate the exposure proportion of Mg-suite per crater examined to be 0.52. We calculate the farthest neighboring detection for a given identification to be  $5103 \pm 243$  km, which is nearly half the circumference of the Moon (5460 km, or the maximum farthest neighbor distance achievable) indicating that the Mg-suite is not regionally constrained.

### 2.1. Melt Volume

All model cases of CMO-induced partial melting successfully meet Constraint 1. In general, downwelling of thicker ilmenite-bearing cumulate (IBC) layers leads to greater melt volumes derived from the responsive upwelling of the lower mantle. The IBC-mantle viscosity contrast (hereafter, viscosity contrast) does not systematically correlate with total melt volume (Fig. 2a). Model runs with IBC thicknesses of 30 km (Runs 1–5) yield total melt volumes ranging from 10.0–5.6 vol.% of the lunar crust, whereas runs with IBC thicknesses of 50 km (Runs 6–9) yield 17.2–13.2 vol.% (Table 1). Runs 10 (IBC = 100 km) and 11 (IBC = 150 km) resulted in melt volumes proportional to 25.6 and 18.3 vol.% of the lunar crust, respectively.

## 2.2. Magmatic Duration and Formation Interval

Magmatic durations (full width at half maximum of peak melt production) and formation intervals (time measured from the onset of the model to 50% cumulative melt volume) are both negatively correlated with viscosity contrast for a given IBC thickness (supplementary Figs. 1, 2). Likewise, for a given mantle reference viscosity, models with thicker IBC result in shorter magmatic durations and formation intervals. Cases with low mantle reference viscosity result in shorter magmatic durations and formation intervals compared to those using our high mantle reference viscosity, if viscosity contrast and IBC thickness are controlled for (Fig. 2b,c). Magmatic durations for Runs 1–5 (IBC = 30 km) range between 69.2–2.5 Myrs, and with formation intervals between 155.9–14.7 Myrs (Table 1). For Runs 6–9 (IBC = 50 km), the magmatic durations and formation intervals range from 20.2–3.5 Myrs and 55.6–12.1 Myrs, respectively. Runs 10 and 11 (IBC = 100 km and 150 km, respectively) resulted in magmatic durations of 3.1 and 1.8 Myrs, and with formation intervals of 6.4 and 3.9 Myrs.

## 2.3. Spatial Analysis

Most all cases exhibit a global upwelling pattern (e.g., Run 9, Fig. 3; additional cases are displayed in supplementary Fig. 3). Run 11 was the only model with a hemispherical concentrated IBC downwelling. Figure 3 showcases the responding morphology and melting of upwelling lower mantle in two examples; Run 9 (IBC = 50 km) and Run 11 (IBC = 150 km). Specifically, we isolate a time slice near peak melt production to visualize the 2-D morphology of upwelling Layer 0 and associated regions of melting. Additionally, we present a 2-D slice of the downwelling IBC overlain by a visualization of the 3-D melt surface of Layer 0. These visualizations demonstrate the upwelling and melting response of the lower mantle to various patterns of IBC downwelling.

To make the comparison between natural observation and model, we randomly sample the surface of our models 164 times to replicate the number of craters investigated by<sup>21</sup>. Each sampling location is a synthetic crater, and the area sampled by the synthetic crater is determined by the scaling relationship between central peak and crater diameter as reported by<sup>33</sup> and using the crater diameters reported by<sup>21</sup>. If melt from Layer 0 is present in a sampled area, we tally an identification of Mg-suite (Fig. 3). We then sum the number of Mg-suite identifications over the 164 random samplings to quantify the synthetic exposure proportion. A thousand iterations are performed with randomized cratering locations that define an average synthetic exposure proportion in addition to an average farthest neighbor distance (each with an associated standard deviation for every dynamical scenario). Our model includes a 2% melt detection threshold (i.e., melting in excess of 2% is sufficient to be mobilized and detected), and therefore represents an efficient system of melt extraction from depth and high detectability. To test the effects of decreasing efficiency, we increase the melt detection threshold (MDT) in 1% increments (up to 7%) and run the same 1000 random cratering iterations for each percentage step. The resulting data can be taken to evaluate the effects on global melt distribution within an efficient (MDT = 2–3%), moderate (MDT = 4–5%), and a less-efficient (MDT = 6–7%) system of melt extraction and detection.

In general, melts derived from the upwelling of lower mantle cumulates in response to CMO can explain the global spatial constraints (Table 1). Most runs co-satisfy the distance and exposure constraints at low to moderate MDT = 3–5%. Run 11, with its relatively thick IBC layer (150 km), is the only model that failed to simultaneously satisfy the farthest neighbor and exposure proportion over the entire range of MDT considered.

## 3. Discussion

### 3.1. Abundance, timing, and spatial extent of initial secondary crust building

We first emphasize that our model of CMO does not require KREEP to explain the abundance, timing, and extent of Mg-suite rocks. Previous work has criticized the limited extent of KREEP-free partial melting during CMO as a shortcoming for Mg-suite petrogenesis<sup>12</sup>. However, all cases modeled here generated melt volumes proportional to ~ 6–26 vol.% of the lunar crust (Fig. 4a). Constrained by geologically realistic initial conditions and dynamical parameters, our modeling therefore demonstrates that the modest fraction of Mg-suite within the lunar crust (~ 6–30 vol.%) is well explained by CMO-induced partial melting of the lower mantle. In this context, we suggest that, while KREEP may have contributed to the petrogenesis of a subset of Mg-suite samples, it is not necessary for the initiation of secondary crust building on the Moon<sup>10,11,16</sup>.

The CMO process alone can also reconcile the near-concordant formation ages between the primary flotation crust (FAN) and secondary Mg-suite (Fig. 4a). Chronological constraints used in this study are derived from concordant dating of Mg-suite rocks and the near-concordant ages of FAN<sup>8</sup>. Collectively, these data indicate a relatively short magmatic duration for Mg-suite and a brief formation interval relative to FAN production. A major result is that our modeling naturally aligns with these two chronological constraints, as we demonstrate that magmatic duration and formation intervals are positively correlated phenomena for CMO-induced magmatism (Fig. 4a). Specifically, Fig. 4a demonstrates that CMO scenarios capable of explaining the brief duration of Mg-suite magmatism ( $\leq 18$  Myrs) also result in formation intervals  $\leq 37$  Myrs. In this way, the short formation interval and brief magmatic duration of the Mg-suite revealed by geochronology is naturally explained by IBC-driven CMO. If instead large amounts of radiogenic heat contributed to KREEP-induced melting of the Mg-suite source, this prolonged source of heating should extend the formation interval between FAN and Mg-suite beyond current constraints and further questions the role of KREEP in driving early secondary crust building.

Implicit in the near-concordant dates of FAN is that the LMO solidified near 4360 Ma. Other chronological approaches suggest LMO solidification occurred earlier, and perhaps as early as 4510 Ma<sup>34,35</sup>. If the earlier LMO solidification dates are accurate, this would require CMO-induced Mg-suite formation intervals of ~ 100–150 Myrs. Our models with a relatively thin IBC layer (30 km thick) and small viscosity contrast ( $\geq 10^{-2}$ ) produce formation intervals on this timescale (Fig. 2c), but they also result in magmatic

durations that are longer (37–69 Myrs) than the current constraint of 18 Myrs (Fig. 2b). In this context, we stress that thin IBC layers should be most enriched in ilmenite. Because ilmenite is rheologically weak, a thin IBC layer and low viscosity contrast is not a geologically or experimentally favored parameter combination<sup>36</sup>. Our higher viscosity contrast ( $\leq 10^{-3}$ ) models are therefore better aligned with rheological expectations and uniformly produce magmatic durations that are  $< 18$  Myrs. Reconciling an older FAN formation age ( $\sim 4.5$  Ga) with Mg-suite petrogenesis by IBC-driven CMO may require future revisions to lunar geochronology and the rheology of LMO cumulates. Whereas we show that a younger FAN and near concordant secondary crust building is entirely consistent with current geochronological and rheological constraints.

We note also that lowering the reference viscosity of the mantle serves to decrease both the formation interval and magmatic duration of early secondary crust building (Fig. 2b,c). The range of reference viscosities taken here are consistent with a dry peridotite rheology<sup>32</sup>, but it is possible that water<sup>37–42</sup> and trapped melt<sup>43–45</sup> act to lower cumulate viscosity within the LMO<sup>46,47</sup>. If this were the case, then the observed short formation interval and magmatic duration could be satisfied over a wider parameter space than documented here. Following, a rheologically weaker cumulate pile poses additional difficulties for reconciling early dates of LMO solidification given the apparent requirement for both a longer formation interval and extended magmatic duration.

Our spatial analysis indicates that lower mantle melting in response to IBC-driven CMO can co-satisfy the global constraints from orbital remote sensing of Mg-suite (Fig. 4b). Our dynamical modeling specifically identifies that overturn of a thin to moderately thick ilmenite-bearing cumulate ( $\sim 30$ -50km, possibly up to 100 km) can reproduce the key volume, geochronological, and spatial characteristics of the Mg-suite when considering a high viscosity contrast ( $10^{-3} - 10^{-4}$ ) with the underlying mantle. Our results eliminate thick IBC layers (150 km) and degree-1 downwelling as a viable scenario because the responding hemispheric melt distribution of Run 11 violates the coupled exposure and distance constraints of Mg-suite (Fig. 4b). Our results are therefore most consistent with numerical and experimental simulations of the LMO, which suggest relatively thin IBC layers ( $\sim 10$ –50 km) based on mass balance and phase equilibria<sup>5,32,48,49</sup>. Thicker IBC layers up to 150 km are expected when considering the dynamic redistribution and coalescence of small IBC diapirs during the LMO solidification process<sup>7,32</sup>, and our modeling therefore suggests this secondary processing of the IBC layer did not occur.

It is for these reasons that we conclude CMO-induced melting of KREEP-poor primary mantle cumulates can simultaneously explain the origin, abundance, timing, duration, and spatial extent of Mg-suite magmatism (Fig. 4). By extension, our CMO model provides explanation for the rapid transition from primary to secondary crust building on the Moon. Finally, the Mg-suite provides foundational evidence for the hypothesis that gravitational instabilities in magma ocean cumulate piles are major driving forces for the dynamics of early mantle convection within differentiated bodies<sup>7,50,51</sup>. Our work supports this hypothesis and implies that the influence of magma oceans remains central to planetary evolution, even after their solidification is complete.

## Declarations

# ACKNOWLEDGMENTS

The authors are grateful to Lin Li for sharing the spectroscopic dataset used in this study. TCP expresses his gratitude for the Gordon McKay Fellowship in support of this international collaboration and acknowledges the JETS contract at NASA Johnson Space Center. Computational work was supported by resources provided within the High Performance Computing Platform of Peking University. [Acknowledge editor and reviewers]. [OTHER]. LPI Contribution No. [ADD IF ACCEPTED]. LPI is operated by USRA under co-operative agreement with the Science Mission Directorate of the National Aeronautics and Space Administration.

## References

1. Elkins-Tanton, L.T. Magma oceans in the inner solar system. *Ann. Rev. Earth Planet. Sci.*, **40**, 113-139 (2012).
2. Warren, P.H. The magma ocean concept and lunar evolution. *Ann. Rev. Earth Planet. Sci.* **13**, 201-240 (1985).
3. Hess, P.C. Petrogenesis of lunar troctolites. *J. Geophys. Res.*, **99**, 19083-19093 (1994).
4. Longhi, J., Durand, S.R., Walker, D. The pattern of Ni and Co abundances in lunar olivines. *Geochim. Cosmochim. Acta* **74**, 784-798 (2010).
5. Elardo, S.M., Draper, D.S., Shearer, C.K. Lunar magma ocean crystallization revisited: bulk composition, early cumulate mineralogy, and the source regions of the highlands Mg-suite. *Geochim. Cosmochim. Acta* **75**, 3024-3045 (2011).
6. Prissel, T.C., Parman, S.W., Head J.W. Formation of the lunar highlands Mg-suite as told by spinel. *Am. Mineral.* **101**, 1624-1635 (2016a).
7. Hess, P.C., Parmentier, E.M. A model for the thermal and chemical evolution of the Moon's interior: implications for the onset of mare volcanism. *Earth Planet. Sci. Lett.* **134**, 501-514 (1995).
8. Borg, L.E. et al. The formation and evolution of the Moon's crust inferred from the Sm-Nd isotopic systematics of highlands rocks. *Geochim. Cossmochim. Acta.* **290**, 312-332 (2020).
9. Zhang, B., et al. Timing of lunar Mg-suite magmatism constrained by SIMS U-Pb dating of Apollo norite 78238. *Earth Planet. Sci. Lett.*, **569**, 117046 (2021).
10. Shearer, C.K., et al. Origin of the lunar highlands Mg-suite: an integrated petrology, geochemistry, chronology, and remote sensing perspective. *Am. Mineral.* **100**, 294-325 (2015).
11. Prissel, T.C., and Gross, J. On the petrogenesis of lunar troctolites: New insights in to cumulate mantle overturn and mantle exposures in impact basins. *Earth Planet. Sci. Lett.*, **551**, 116531 (2020).
12. Elardo, S.M. Laneuville, M., McCubbin, F.M., Shearer, C.K. Early crust building enhanced on the Moon's nearside by mantle melting-point depression. *Nat. Geosci.*, **13**, 339-343 (2020).

13. Nelson, W.S., Hammer, J.E., Shea, T., Hellbrand, E., Jeffrey Taylor, G. Chemical heterogeneities reveal early rapid cooling of Apollo Troctolite 76535. *Nat. Comm.*, **12**, 7054 (2021).
14. Jolliff, B.L., Gillis, J.J., Hasking, L.A., Korotev, R.L., Wieczorek, M.A. Major lunar crustal terranes: surface expressions and crust-mantle origins. *J. Geophys. Res.*, **105**, 4197-4216 (2000).
15. Wieczorek, M.A., & Phillips, R.J. The 'Procellarum KREEP Terrane': implications for mare volcanism and lunar evolution. *J. Geophys. Res.*, **105**, 20417-20430 (2000).
16. Gross, J., Hilton, A., Prissel, T.C., Setera, J.B., Korotev, R.L., Calzada-Diaz, A. Geochemistry and petrogenesis of Northwest Africa (NWA) 10401: a new type of the Mg-suite rocks. *J. Geophys. Res. Planets*, **125**, e2019JE006225 (2020).
17. Treiman, A.H., Maloy, A.K., Shearer, C.K., Gross, J. Magnesian anorthositic granulites in lunar meteorites Allan Hills A81005 and Dhofar 309: Geochemistry and global significance. *Meteorit. Planet. Sci.*, **45**, 163-180 (2010).
18. Gross, J., and Treiman, A.H. Unique spinel-rich lithology in lunar meteorite ALHA 81005: Origin and possible connection to M3 observations of the farside highlands. *J. Geophys. Res.* **116**, E10009 (2011).
19. Tompkins, S., Pieters, C.M. Mineralogy of the lunar crust: results from Clementine. *Meteorit. Planet. Sci.* **34**, 25-41 (1999).
20. Pieters, C.M., et al. The distribution of Mg-spinels across the Moon and constraints on crustal origin. *Am. Min.*, **99**, 1893-1910 (2014).
21. Sun, Y., Lin, L., Zhang, Y. Detection of Mg-spinel bearing central peaks using M3 images: implications for the petrogenesis of Mg-spinel. *Earth Planet. Sci. Lett.*, **465**, 48-58 (2017).
22. Edmunson, J., Borg L.E., Nyquist, L.E., Asmeron, Y. A combined Sm-Nd, Rb-Sr, and U-Pb isotopic study of Mg-suite norite 78238: further evidence for early differentiation of the Moon. *Geochim. Cosmochim. Acta*, **73**, 514-527 (2009).
23. Borg, L.E. et al. Evidence that the Moon is either young or did not have a global magma ocean. *Nature* **477**, 70-72 (2011).
24. Carlson, R.W., Borg, L.E., Gaffney, A.M., and Boyet, M. Rb-Sr, Sm-Nd and Lu-Hf isotope systematics of the lunar Mg-suite: the age of the lunar crust and its relation to the time of Moon formation. *Phil. Trans. Roy. Soc.* **A372**, 20130246 (2014).
25. Sio, C.K., Borg, L.E., Cassata, W.S. The timing of lunar solidification and mantle overturn recorded in ferroan anorthosite 62237. *Earth Planet. Sci. Lett.*, **538**, 116219 (2020).
26. Borg, L.E., Gaffney, A.M., Shearer, C.K. A review of lunar chronology revealing a preponderance of 4.34-4.37 Ga ages. *Meteor. Planet. Sci.* **50**, 715-732 (2015).
27. Jackson, C.R.M., et al. Visible-infrared spectral properties of iron-bearing aluminate spinel under lunar-like redox conditions. *Am. Min.*, **99**, 1821-1833 (2014).
28. Prissel, T.C., et al. Pink Moon: The petrogenesis of pink spinel anorthosites and implications concerning Mg-suite magmatism. *Earth Planet. Sci. Lett.*, **403**, 144-156 (2014).

29. Prissel, T.C., Whitten, J.L., Head, J.W., Parman, S.W. On the potential for lunar highlands Mg-suite extrusive volcanism and implications concerning crustal evolution. *Icarus*, **277**, 319-329 (2016b).
30. Williams, K.B., et al. Reflectance spectroscopy of chromium-bearing spinel with application to recent orbital data from the Moon. *Am. Min.*, **101**, 726-734 (2016).
31. Wieczorek, M.A., Zuber, M.T. The composition and origin of the lunar crust: Constraints from central peaks and crustal thickness modeling. *Geophys. Res. Lett.*, **28**, 4023-4026 (2001).
32. Li, H., Zhang, N., Liang, Y. Lunar cumulate mantle overturn: a model constrained by ilmenite rheology. *J. Geophys. Res. Planets.*, **124**, 1357-1378 (2019).
33. Hale, W., Head, J.W. Central peaks in lunar craters: Morphology and morphometry. *Proc. Lunar Planet. Sci. Conf.* **10**, 2623-2633 (1979).
34. Barboni, M. et al. Early formation of the Moon 4.51 billion years ago. *Sci. Adv.* **3** (2017).
35. Maurice, M., et al. A long-lived magma ocean on a young Moon. *Sci. Adv.* **6**, eaba8949 (2020).
36. Dygert, N., Hirth, G., Liang, Y. A flow law for ilmenite in dislocation creep: Implications for lunar cumulate mantle overturn. *Geophys. Res. Lett.*, **43**, 532-540 (2016).
37. Saal, A., et al. Volatile content of lunar volcanic glasses and the presence of water in the Moon's interior. *Nature*, **454**, 192-195 (2008).
38. Saal, A., et al. Hydrogen isotopes in lunar volcanic glasses and melt inclusions reveal a carbonaceous chondrite heritage. *Science*, **340**, 1317-1320 (2013).
39. McCubbin, F.M. et al. Nominally hydrous magmatism on the Moon. *Proc. Nat. Acad. Sci.* **107**, 11223-11228 (2010).
40. Hui, H. et al. Water in lunar anorthosites and evidence for a wet early Moon. *Nature Geosci.* **6**, 177-180 (2013).
41. Hauri, E. et al. Origin and evolution of water in the Moon's interior. *Ann. Rev. Earth Planet. Sci.*, **45**, 89-111 (2017).
42. Lin, Y. et al. Evidence for an early wet Moon from experimental crystallization of the lunar magma ocean. *Nat. Geosci.* **10**, 14-18 (2017).
43. Snyder, G.A., Taylor, L.A., Neal, C.R. A chemical model for generating the sources of mare basalts: Combined equilibrium and fractional crystallization of the lunar magmasphere. *Geochim. Cosmochim. Acta*, **56**, 3809-3823 (1992).
44. Elkins-Tanton, L.T., Burgess, S., Yin, Q.-Z. The lunar magma ocean: Reconciling the solidification process with lunar petrology and geochronology. *Earth Planet. Sci. Lett.*, **304**, 326-336 (2011).
45. McCubbin, F.M., et al. Magmatic volatiles (H, C, N, F, S, Cl) in the lunar mantle, crust and regolith: abundances, distributions, processes, and reservoirs. *Am. Mineral.*, **100**, 1668-1707 (2015).
1. Elkins-Tanton, L.T., Grove, T.L. Water (hydrogen) in the lunar mantle: Results from petrology and magma ocean modeling. *Earth Planet. Sci. Lett.*, **307**, 173-179 (2011).

47. Hirth, G., Kohlstedt, D.L. Water in the oceanic upper mantle: implications for rheology, melt extraction and the evolution of the lithosphere. *Earth Planet. Sci. Lett.*, **144**, 93-108 (1996).
48. Rapp, J., Draper, D. Fractional crystallization of the lunar magma ocean: Updating the dominant paradigm. *Meteor. Planet. Sci.* **53**, 1432-1455 (2018).
49. Charlier, B., Grove, T.L., Namur, O., Holtz, F. Crystallization of the lunar magma ocean and the primordial mantle-crust differentiation of the Moon. *Geochim. Cosmochim. Acta*, **234**, 50-69 (2018).
50. Elkins-Tanton, L.T., Parmentier, E.M., Hess, P.C. Magma ocean fractional crystallization and cumulate overturn in the terrestrial planets: Implications for Mars. *Meteorit. Planet. Sci.*, **38**, 1753-1771 (2003).
51. Boukaré, C.-E., Parman, S.W., Parmentier, E.M., Anzures, B.A. Production and preservation of sulfide layering in Mercury's mantle. *J. Geophys. Res. Planets*, **124**, 3354-3372 (2019).
52. Hare, T.M., et al. Image mosaic and topographic map of the Moon: U.S. Geological Survey Scientific Investigations Map 3316, 2 sheets (2015).

## 4. Online Methods

### 4.1 Modeling Parameters

Our model considers downwelling driven by the dense IBC layer within a fully solidified Moon. Overturn driven by dense silicates in a partially solidified Moon<sup>45</sup> is not considered here because it is unclear if this process took place after the isotopic closure of ferroan anorthosites (FANs), which is required for geochronology and the plutonic nature of the Mg-Suite<sup>8</sup>.

Our model Moon includes five layers: core, lower mantle (Layer 0), upper mantle (Layer 1), ilmenite-bearing cumulate layer (IBC, Layer 2), and crust (Layer 3), from bottom to top. The core is only energetically coupled with the lower mantle<sup>32,46</sup>. The IBC has lower viscosity and higher density than the mantle and is overlain by a less dense crust. We set the core-mantle boundary, the lower-upper mantle boundary, the IBC bottom, and the IBC-crust boundary at the nominal radii of 340 km, 1040 km, 1660 km, and 1710 km, respectively. Following previous work<sup>32</sup>, we treat the initial thickness of the IBC layer as a free parameter by modeling cases of 30, 50, 100, and 150km to explore the dynamic return flow patterns and timing of upwelling mantle from Layer 0.

The viscosity contrast between the IBC layer and the underlying mantle plays a key role in determining the dynamics of CMO<sup>36,47-49</sup>. Model viscosity is both temperature and compositionally dependent. Here we explore a range of IBC viscosities constrained by experiments<sup>36</sup>. The predicted viscosity of pure ilmenite is ~4 orders of magnitude lower than that of dry harzburgite (approximated by dry olivine). Mantle Layers 0 and Layer 1 therefore assume the rheology of dry harzburgite, ranging from  $5 \times 10^{20}$  -  $10^{21}$  Pa s, and we vary the viscosity contrast of the IBC layer to be between  $10^{-1}$  -  $10^{-4}$  × that of dry harzburgite<sup>32</sup>.

Instability is induced via random distribution of chemical tracers<sup>50</sup>, meaning we assign no initial perturbation to the IBC-mantle interface. The evolution of the four silicate layers is solved with

conservation of mass, momentum, and energy. The formulation and parameterization of melt generation have been described in<sup>32</sup>. Our mantle solidus is defined by<sup>38</sup>. The mantle thermal Rayleigh number<sup>32</sup> is given to  $6 \times 10^5$ . We apply parameterized equations of<sup>51</sup> to solve for the local production of melt using the mantle solidus from<sup>38</sup>. We first assume that melting in excess of 2% is mobilized and is detectable in the crust by remote techniques<sup>11</sup>, and later increase this threshold as a free parameter in our spatial analysis (detailed further in our results). Our model uses a  $12 \times 64 \times 48 \times 48$  mesh based on CitcomS<sup>52</sup>, which gives an azimuthal resolution of 14 km and radial resolution of 22 km. The ilmenite fraction of the IBC layer is  $\sim 6$ -12 wt% over the range of IBC thicknesses<sup>32</sup>.

Following previous work<sup>46,53,54</sup>, our model assumes 50% of all heat producing elements (U, Th, and K) are present in the IBC layer<sup>7</sup>, while the remaining 50% is evenly distributed throughout the lunar mantle. The heat generation rate of these heat producing elements is calculated based on the bulk U and Th abundances of the Moon. The bulk U and Th abundances of the present day are taken as 25.7 and 102.8 ppb (Th/U = 4), respectively<sup>55</sup>. The Moon is highly depleted of the volatile element K<sup>56-58</sup>. We use the K/Th ratio of 2,500<sup>59</sup>. Additional details of our model are found in<sup>32</sup>.

## 4.2 Natural Constraints

Constraint 1 (Mg-suite volume) is defined by the estimated amount of Mg-suite material within the lunar crust. Although loosely constrained, a modest fraction of the lunar crust is estimated to be comprised of Mg-suite material, constituting as much as  $\sim 6$ -30 vol.% of the lunar crust<sup>19,31</sup>. We therefore consider the total melt volume generated by each model case in relation to the total volume of the lunar crust. We note that the total melt volumes reported here represent a conservative estimate as some Mg-suite melts may have assimilated crust in producing more Mg-suite material<sup>11,60</sup>. The reference volume of the lunar crust is estimated by assuming a spherical shell and using an average crustal thickness of 40 km<sup>61</sup>.

Constraint 2 (magmatic duration) is defined by the estimated duration of Mg-suite magmatism. Recent geochronological results for the Mg-suite tightly constrains magmatic events to occur within  $\pm 9$  Myrs<sup>8</sup>. The variance associated with the Mg-suite age of crystallization could reflect a real distribution of crystallization ages among each sample measured, or it could be attributed to analytical uncertainty. If the latter, then the real duration of Mg-suite crystallization would be even shorter than defined above. We therefore treat the  $\sim 18$  My variance defined by<sup>8</sup> as our duration constraint. We approximate the duration of mantle melting in our dynamical models using the full width at half maximum (FWHM) of melt production rates (Supplementary Fig. 1). Constraint 3 (formation interval) is defined by the maximum interval of time between the ages of FANs secondary Mg-suite samples (including the respective variance associated with each age). The most reliable crystallization ages stated in our introduction (Mg-suite:  $4340 \pm 9$  Myrs, anorthositic crust:  $4359 \pm 9$  Myrs) constrains the formation interval to  $\leq 37$  Myrs<sup>8</sup>. We note that this formation interval includes the time associated with IBC-layer formation following isotopic closure of the crust, magmatic emplacement, and cooling to the closure temperatures associated with the isotopic systems used to date the Mg-suite samples. Our model estimates the time of magmatic

emplacement, prior to cooling and isotopic closure. The IBC layer is also fully formed at time zero in our model. In this study, we consider the interval between time zero of the model and the time step most closely associated with 50% of the cumulative melt volume for each case. The time to 50% cumulative melt volume therefore provides a relatively conservative estimate for the timing of Mg-suite formation compared to the onset of melting in each model. Models reaching 50% cumulative melt volume after 37 My are deemed unsuccessful based on Constraint 3 (Supplementary Fig. 2).

Constraints 4 and 5 (exposure proportion and distance, respectively) account for the spatial distribution of Mg-Suite rocks. We take the spatial distribution of exposed Mg-Suite rocks from<sup>21</sup>. This study examines the mineralogy exposed in 164 craters across the global surface (33-199 km in diameter). Our selection of their dataset is based on their extensive search of craters and basins and the use of a common approach to mineral identification. Here, craters exhibiting spectral signatures of olivine, orthopyroxene, and spinel, with no evidence for clinopyroxene (i.e., a marker for mare basalts) are considered positive Mg-suite detections (Fig. 1). The Mg-suite exposure proportion based on the dataset of<sup>21</sup> is 0.52 detections per crater examined.

Although the complete distribution of subsurface Mg-suite is unknown, the observed spatial distribution of Mg-suite detections can be quantified by measuring the current distance between each detection and its farthest neighbor (Constraint 5). If Mg-suite detections are confined to a small region of the Moon, the farthest neighbor distance for each detection will be relatively short compared to if Mg-suite is more globally distributed. We calculate the average farthest neighbor of observed Mg-suite rocks to be  $5103 \pm 243$  km, which is nearly half the circumference of the Moon (~5460 km, or the maximum farthest neighbor distance achievable) indicating a broad distribution of Mg-suite exposures across the global surface (Fig. 1).

## References

53. Boukaré, C.-E., Parmentier, E.M., Parman, S. Timing of mantle overturn during magma ocean solidification. *Earth Planet. Sci. Lett.*, **491**, 216-225 (2018).
54. Zhang, N., Parmentier, E.M., Liang, Y. A 3D numerical study of the thermal evolution for the Moon after cumulate mantle overturn: The importance of rheology and core solidification. *J. Geophys. Res. Planets*, **118**, 1789-1804 (2013a).
55. Elkins-Tanton, L.T., Van Orman, J.A., Hager, B.H., and Grove, T.L. Reexamination of the lunar magma ocean cumulate overturn hypothesis: melting or mixing is required. *Earth Planet. Sci. Lett.*, **196**, 249-259 (2002).
56. Parmentier, E.M., Zhong, S., Zuber, M.T. Gravitational differentiation due to initial chemical stratification: Origin of lunar symmetry by the creep of dense KREEP. *Earth Planet. Sci. Lett.*, **201**, 473-480 (2002).

57. Zhao, Y., de Vries, J., van den Berg, V., Jacobs, M., van Westrenen, W. The participation of ilmenite-bearing cumulates in lunar mantle overturn. *Earth Planet. Sci. Lett.*, **511**, 1-11 (2019).
58. Scheinberg, A., Elkins-Tanton, L., Zhong, S. Timescale and morphology of Martian mantle overturn. *J. Geophys. Res. Planets.* **119**, 454-467 (2014).
59. Katz, R. Spiegelman, M. Langmuir, C. A new parameterization of hydrous mantle melting. *Geochem. Geophys. Geosys.*, **4**, 1073 (2003).
60. Zhong, S., et al. A benchmark study on mantle convection in a 3-D spherical shell using CitcomS. *Geochem. Geophys. Geosys.* **9**, Q10017 (2008).
61. Zhong, S. Parmentier, M., Zuber, M. A dynamic origin for the global asymmetry of lunar mare basalts. *Earth Planet. Sci. Lett.*, **177**, 131-140 (2000).
62. Zhang, N., Parmentier, E.M., Liang, Y. Effects of lunar cumulate mantle overturn and megaregolith on the expansion and contraction history of the Moon. *Geophys. Res. Lett.*, **40**, 5019-5023 (2013b).
63. Taylor, R.S. *Planetary Science: A lunar perspective*, (p. 481). Houston, Texas: Lunar Planet. Inst (1982).
64. Jones, J.H. Palme, H. Geochemical constraints on the origin of the Earth and Moon. In R. Canup, and K. Righter (Eds.), *Origin of the Earth and Moon* (pp. 197-216). Tuscon: Univ. of Ariz. Press (2000).
65. Albarede, F., Albalat, E. Lee, C.-T. An intrinsic volatility scale relevant to the Earth and Moon and the status of water in the Moon. *Meteorit. Planet. Sci.* **50**, 568-577 (2014).
66. Wang, K., Jacobsen, S. Potassium isotopic evidence for a high-energy giant impact origin of the Moon. *Nature*, **538**, 487-490 (2016).
67. Laneuville, M., et al. Asymmetric thermal evolution of the Moon. *J. Geophys. Res. Planets.* **118**, 1435-1452 (2013).
68. Warren, P.H. Anorthosite assimilation and the origin of the Mg/Fe-related bi-modality of pristine Moon rocks: support for the magmasphere hypothesis. *J. Geophys. Res.* **91**, D331-D343 (1986).
69. Wieczorek, M.A. et al. The crust of the Moon as seen by GRAIL. *Science* **339**, 671-675 (2013).

## Table 1

Table 1 is available in the Supplementary Files section.

## Figures

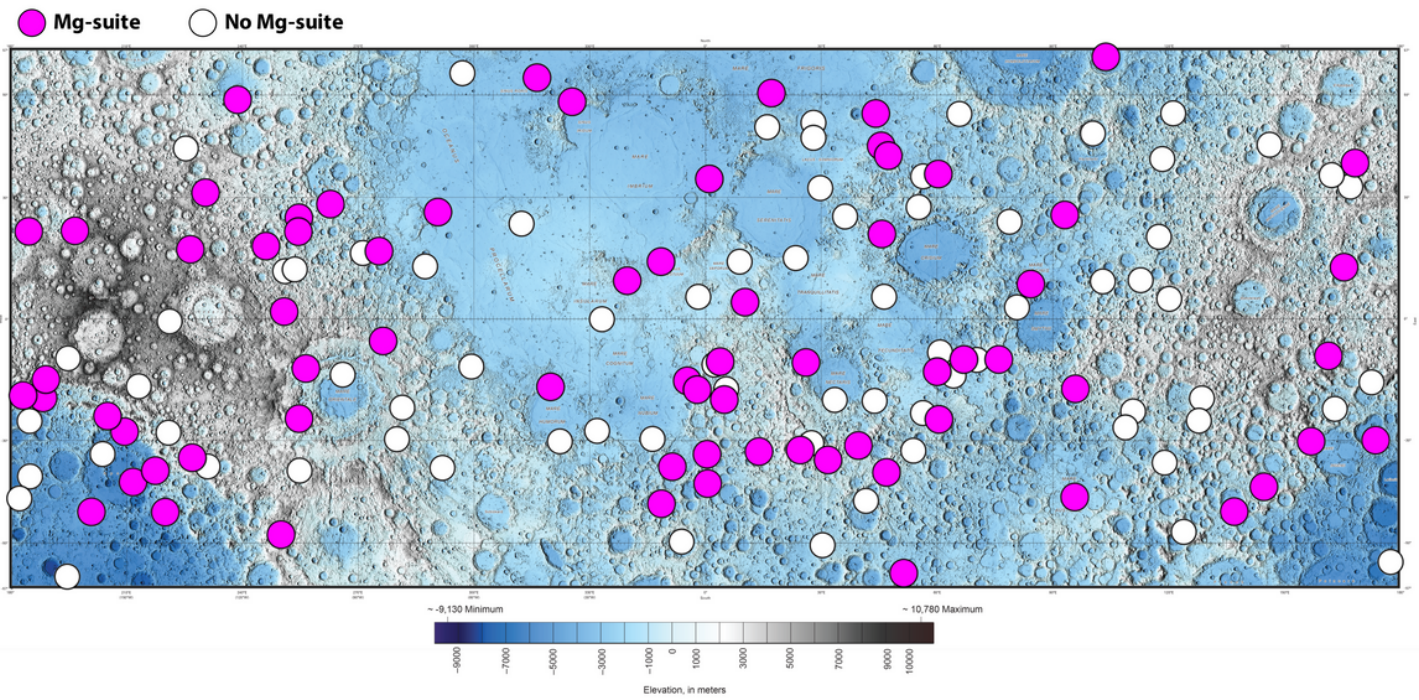


**Figure 1**

**Global extent of candidate Mg-suite exposures.** Topographic base map of the Moon edited from<sup>44</sup>. Mercator projection centered at 0° longitude and between latitudes ± 57°. Color elevation scale provided. Pink-filled circles represent candidate Mg-suite detections (olivine, orthopyroxene, pink spinel) and white-filled circles are craters examined with no detection of Mg-suite from the orbital remote sensing database of<sup>21</sup> examining 164 craters in total across the surface of the Moon. Further discussion provided in the text.

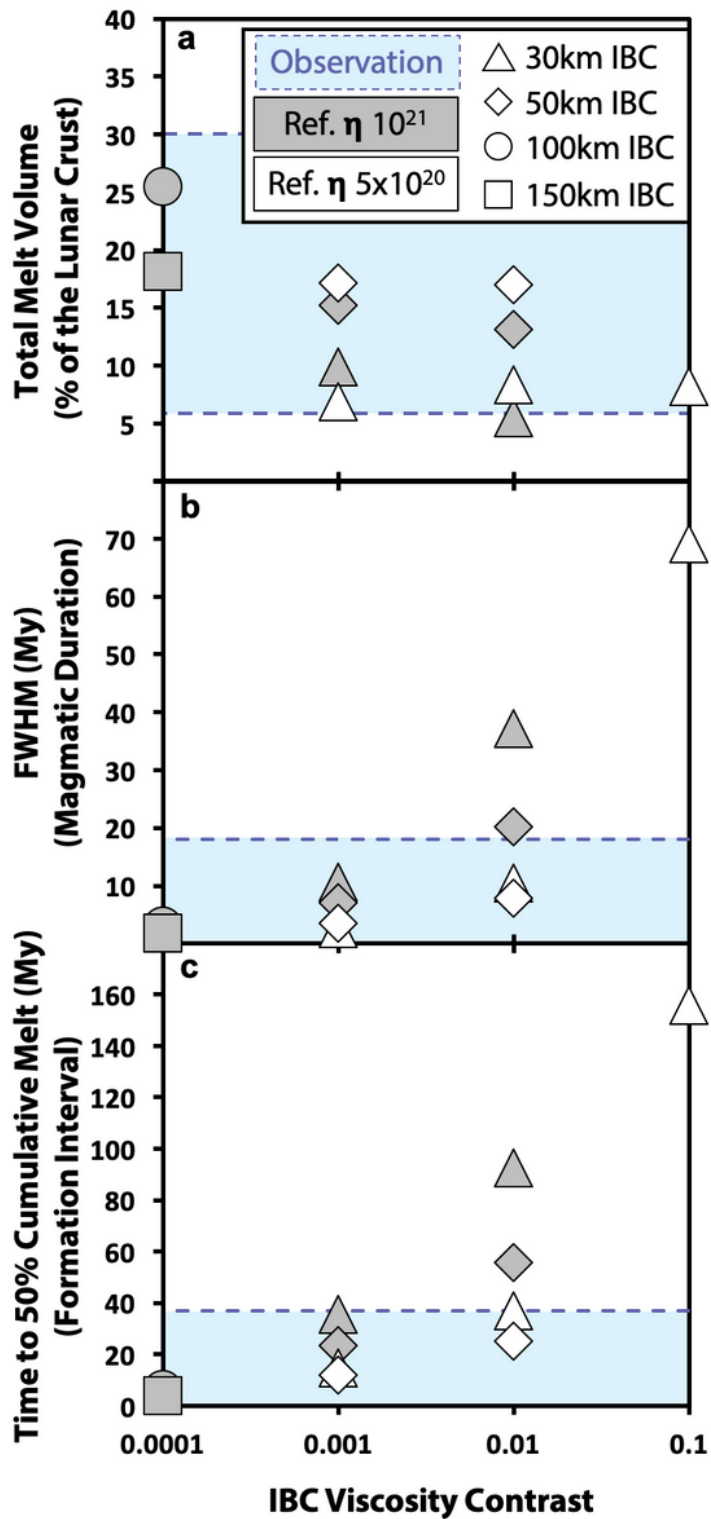
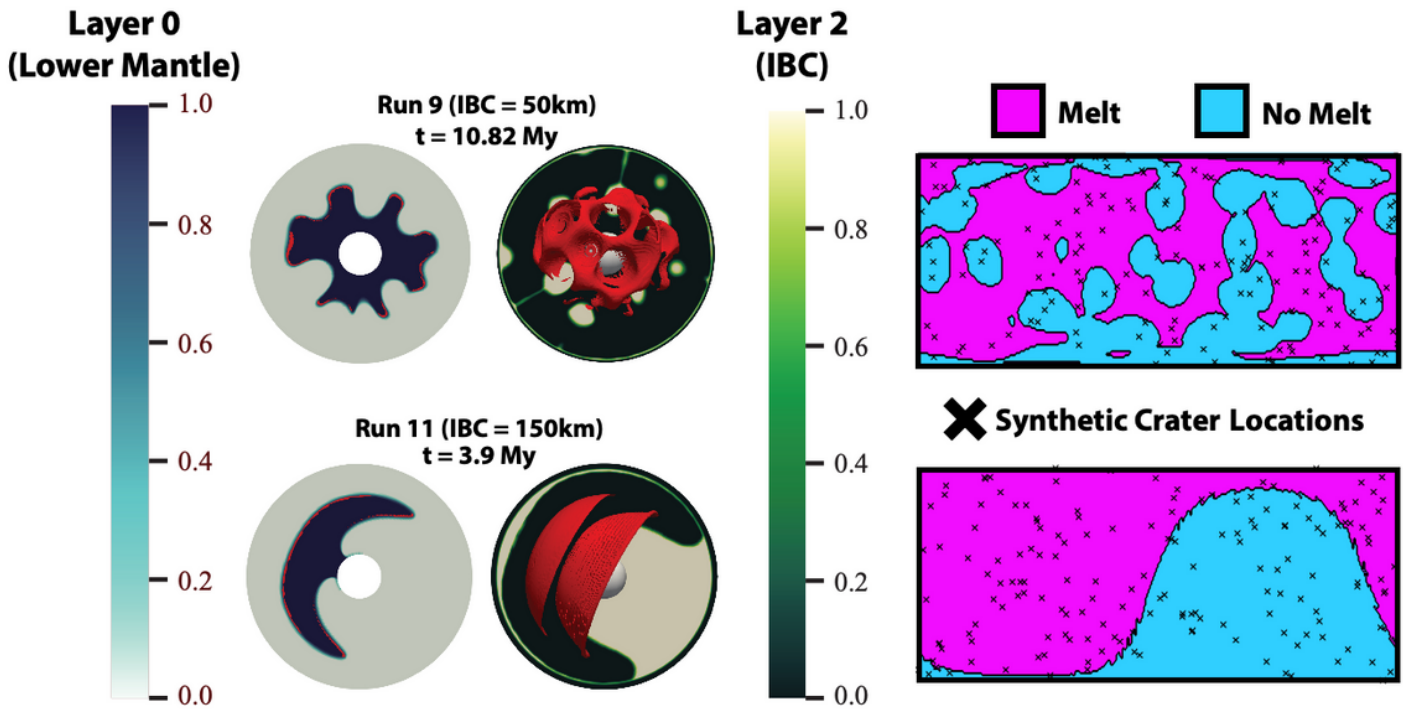


Figure 2

Melt volume and temporal systematics of lower mantle melting in response to cumulate mantle overturn.

(a) the full width at half maximum of peak melt production curves (b), and time to 50% cumulative melt volume (c) plotted as a function of IBC viscosity contrast. Cases with IBC thickness = 30, 50, 100, and 150km are represented by triangles, diamonds, circle, and square, respectively. High reference mantle viscosity = shaded symbols, and low reference mantle viscosity = open symbols. Natural constraints

(defined in our methods) are represented by blue-shaded regions. Overall, an increase in IBC thickness and viscosity contrast generally results in larger total melt volumes (a), briefer periods of magmatic duration (b), and more rapid formation intervals (c). Further discussion presented in the text.



**Figure 3**

**Morphology and melting of upwelling lower mantle in response to cumulate mantle overturn.** Runs 9 (IBC = 50km) and 11 (IBC = 150km) are showcased. Presented are snap shots near peak melt production. Left: isolating the 2-D morphology of upwelling layer 0 (fraction of lower mantle color scale provided) and associated regions of melting (red). Right: visualization of the 3-D melt surface of layer 0 (red) overlain on top of a 2-D slice of the downwelling layer 2 (fraction of IBC color scale provided). Run 9 exhibits a global upwelling pattern, and like most all other cases exhibits a spherical harmonic degree of IBC downwelling  $> 1$  (additional cases found in supplementary Figure 3). Run 11 is the only model that did not result in a global upwelling pattern and was dominated by a spherical harmonic degree of 1 for IBC downwelling. Also shown are the associated 2D melt surface expressions considering a melt detection threshold of 4% with regions of melting (pink), no melting (blue), and synthetic crater locations (x) used to determine exposure proportions and farthest neighboring distances (see also figure 4). Further discussion provided in the text.

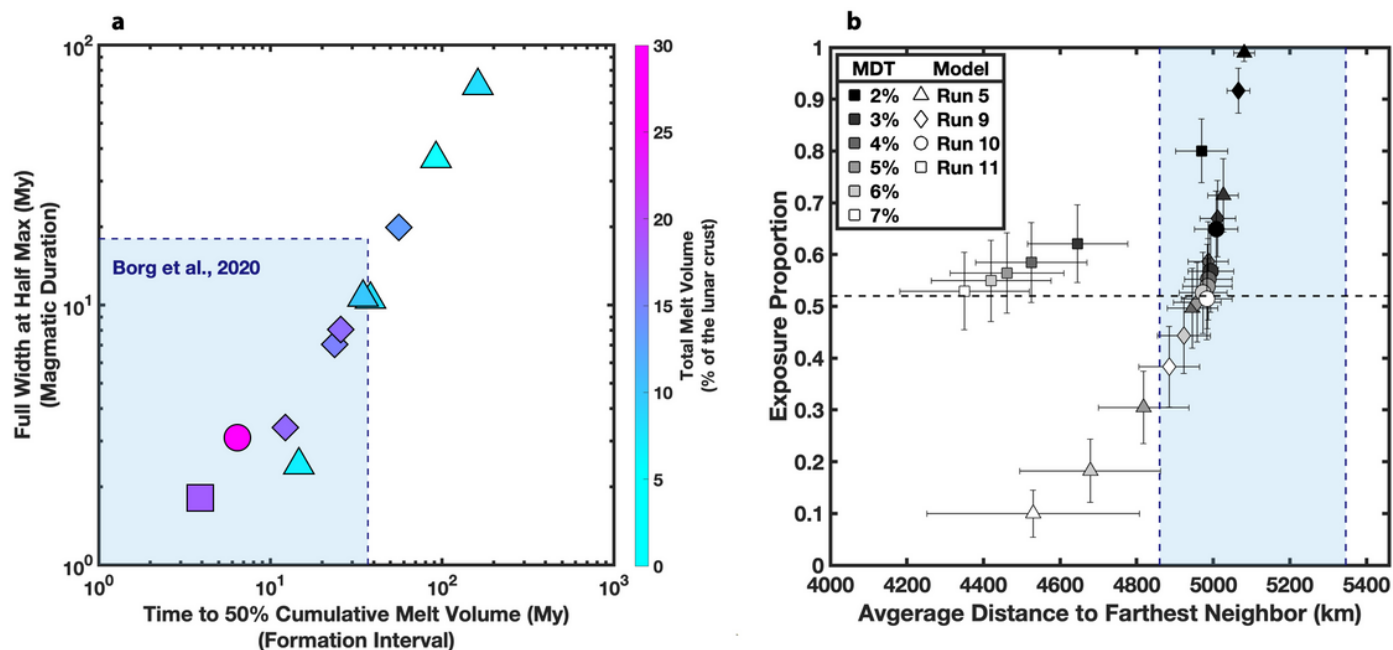


Figure 4

**Temporal and spatial correlations of lower mantle melting induced by cumulate mantle overturn. (a)** FWHM vs. time to 50% cumulative melt volume. Symbols are the same from Fig. 2, but now filled with the associated color scale for total melt volume (reported in vol. % of the total lunar crust). Geochronological constraints from (13) indicate a relatively short magmatic duration and formation interval for Mg-suite petrogenesis (blue-shaded region). Model data shows that magmatic duration and formation intervals are positively correlated phenomena during cumulate mantle overturn. Results indicate cumulate overturn can simultaneously satisfy the onset, abundance, and duration of Mg-suite magmatism. **(b)** Exposure proportion vs. average distance to farthest neighbor. Symbols are the same as Fig. 2, but now filled with gray scale representing each melt detection threshold considered (MDT = 2 – 7%). The observed exposure and distance constraints of Mg-suite detections are plotted as a horizontal dashed line and blue-shaded region, respectively. Apart from Run 11, all cases of cumulate overturn are capable of successfully co-satisfying the exposure and distance constraints when considering the range of MDT explored here. Further discussion provided in the text.

## Supplementary Files

This is a list of supplementary files associated with this preprint. Click to download.

- [NGTable1.pdf](#)
- [TableS1.pdf](#)
- [NGFigS1.png](#)
- [NGFigS2.png](#)
- [NGFigS3.png](#)